PHYSICAL REVIEW MATERIALS **5**, 085003 (2021)

Physical properties of face-centered cubic structured high-entropy alloys: Effects of NiCo, NiFe, and NiCoFe alloying with Mn, Cr, and Pd

Pallab Bag,[1] Yi-Cheng Su,[1] Yung-Kang Kuo,[1,*] Yi-Cheng Lai,[2] and Shyi-Kaan Wu[2]
[1]*Department of Physics, National Dong Hwa University, Hualien 97401, Taiwan*
[2]*Department of Materials Science and Engineering, National Taiwan University, Taipei 10617, Taiwan*

(Received 22 February 2021; accepted 22 July 2021; published 6 August 2021)

This paper reports a comprehensive study of electrical and thermal transport properties of a series of face-centered cubic structured high-entropy alloys by alloying Mn, Cr, and Pd elements in NiCo, NiFe, and NiCoFe alloys. X-ray diffraction revealed a single-phase Cu-type cubic structure, and scanning electron microscopy displayed elongated grained microstructures in all alloys. Like NiCo, NiFe, and NiCoFe alloys, the alloys containing Cr/Mn/Pd exhibit metallic behavior; however, their electrical transport properties, such as residual resistivity, residual resistivity ratio, and temperature coefficient of resistivity, vary significantly due to the increase of chemical disorder and defects. The analysis of resistivity of these alloys further showed different scattering mechanisms at low temperatures. Interestingly, the electrical resistivity of NiCoCr, NiCoFeCr, and NiCoFeMn alloys is nearly linear at low temperatures, most likely related to the Mott-Ioffe-Regel limit. Additionally, the NiCoMnCr and NiCoFeMnCr alloys exhibit a minimum in resistivity at low temperatures, which can be explained by the weak localization effect. The Seebeck coefficient measurements reveal that the charge carrier for thermoelectric transport in NiCo, NiFe, and NiCoFe is changed from electrons to holes with Mn alloying. In contrast, a sign reversal of the charge carriers observed in the Cr-containing alloys is connected to the compensation of electron and hole carriers. Furthermore, the NiCoCr, NiCoFeCr, NiCoMnCr, and NiCoFeMnCr alloys show a negative phonon drag effect at low temperatures due to electron-phonon interaction. The measured thermal conductivity behaves similarly in all alloys, except for a considerable reduction in magnitude in Cr/Mn/Pd-containing alloys. This is attributed to a significant decrease of electronic thermal conductivity due to an increased electron scattering by disorders and lattice distortions and a substantial modification of band structure. There is almost an equal contribution of electronic and lattice to the total thermal conductivity in Cr/Mn/Pd-containing alloys, suggesting a semimetallic nature. The temperature dependence of lattice thermal conductivity of these alloys is described by different phonon scattering mechanisms.

DOI: 10.1103/PhysRevMaterials.5.085003

I. INTRODUCTION

High-entropy alloys (HEAs) have been the subject of increasing interest in the basic sciences, metallurgy, and engineering over the past two decades because of their numerous mechanical, physical, and chemical properties, such as superior phase stability, fracture toughness and ductility [1–4], excellent corrosion and oxidation resistance [5], superconductivity [6], high thermoelectric power and magnetocaloric effect [7,8], short-range chemical ordering [9,10], and soft ferromagnetism [11,12]. HEAs generally possess simple crystal structure, e.g., face-centered cubic (fcc), body-centered cubic, and hexagonal close-packed, and are defined as equiatomic or near equiatomic multiprincipal element metallic systems, where a high configuration entropy by the components reduces the free energy and stabilizes the chemically disordered solid-solution phases [13–18]. In recent studies, the Heusler alloys that consist of three or four elements are also considered HEAs [19,20]. The multifunctional characteristics in HEAs are due to the high entropy of mixing, sluggish diffusion, lattice distortion, and cocktail effects, which originated from the complex local structure and interactions among the constituents [13–16,20–22]. In addition, the role of a particular type of element in these alloys is well considered. Such characteristics cannot be found in the conventional alloys or chemically ordered intermetallic alloys that generally comprise one or two principal elements along with small amounts of various other components (e.g., stainless steels and Ni-based superalloys) [23,24]. Hence, HEAs could be promising candidates for various industrial and technologic applications, including spacecraft, submarines, nuclear reaction, hypersonic activities, and so on [4,8,13–15].

To date, numerous efforts have been explored on the microstructures and mechanical properties in HEAs [1–5,9,13–16,19,20]. However, understanding their physical properties at low and mid temperatures is less studied [25–29]. The electrical, thermal, and magnetic properties of a few Ni-based HEAs in fcc structure were investigated at low temperatures using the midperiod 3*d* transition metals Co, Fe, Cr, Mn, etc., [25,26,29–31], as these HEAs were reported to be of high phase stability and malleability [1,11,20]. The magnetism of the constituents in HEAs was found to play an essential role in determining their physical and mechanical properties, as in

---

[*] Corresponding author: ykkuo@gms.ndhu.edu.tw

the midperiod 3*d* transition metals. In these transition metals, Mn and Cr atoms are antiferromagnetic (AFM), while Fe, Co, and Ni atoms are ferromagnet (FM) in the standard bulk form [25,26,29]. It has been reported that NiCo, NiFe, and NiCoFe alloys consisting of FM metals remained FM above room temperature and exhibited high saturation magnetization. Noticeably, the NiCoFe alloy with alloying Al and Si elements exhibits higher electrical resistivity due to severe lattice distortion, chemical disorder, and malleability, which is an essential requirement for soft magnets [11].

Recent studies have demonstrated that HEAs containing Mn and/or Cr exhibit a wide variety of physical properties, such as spin-glass states [30], frustrated Mn/Cr moments [32,33], longitudinal spin fluctuations [34], lower Curie temperature (T_C) [26,30,35], quantum criticality [36], reduction in mean free path, and lower thermal conductivity [25,26,29,31]. Also, the mechanical properties and thermal expansion were reported to vary significantly upon the addition of Mn/Cr in HEAs [1,37,38]. Theoretical *ab initio* electronic structure calculations suggested that such unusual physical and mechanical properties in HEAs were satisfactorily described by the effects of chemical, magnetic, and lattice disorders of the Mn and Cr atoms [25,26,29,30,39,40]. Furthermore, by alloying nonmagnetic *3d* and *4d* transition elements (e.g., Cu and Pd), the mechanical and physical properties of HEAs can be tailored and improved [35,41,42]. For example, by alloying Cu and Pd in homogenized NiCoFeMn and NiCoFeCr alloys, the magnetic state at room temperature transforms from paramagnetic (PM) to FM, and an increase in saturation magnetization was also observed [41,42]. In this regard, HEAs containing transition metals are the subject of particular interest, and systematic studies on the electrical and thermal transport properties are highly desired.

In this paper, the physical properties of a series of fcc-structured HEAs by alloying Mn, Cr, and Pd elements in NiCo, NiFe, and NiCoFe alloys were investigated via powder x-ray diffraction (XRD), scanning electron microscopy (SEM), microhardness, electrical resistivity (ρ), Seebeck coefficient (S), and thermal conductivity (κ) measurements. The XRD results confirmed that all investigated HEAs formed a single-phase Cu-type fcc structure, and the effective valence electrons concentration is $\geqslant 8$. The SEM study revealed elongated grained microstructures along with lots of shear bands and dislocations in the Mn-, Cr-, and Pd-containing alloys, which further improved the hardness of these alloys. The influence of the alloying of Cr/Mn/Pd elements on the electrical and thermal transport properties of the studied HEAs is discussed. The measurement of $\rho(T)$ and $S(T)$ revealed metallic behavior in all alloys; however, electrical transport properties vary significantly with Cr/Mn/Pd alloying. The $\rho(T)$ of NiCoCr, NiCoFeCr, and NiCoFeMn alloys can be explained within the framework of the Mott-Ioffe-Regel (MIR) limit and can be classified as bad metal. On the other hand, the $\rho(T)$ behavior can be described by a weak localization effect induced by disorder in NiCoCrMn and NiCoFeCrMn. The $S(T)$ of the Cr/Mn/Pd-containing alloys exhibits a small value in S ($<2.5\ \mu$V/K) with different signs, indicating a multiband effect. Also, some of these Cr- and/or Mn-containing alloys exhibit a negative phonon-drag effect at low temperatures. The thermal transport properties by the $\kappa(T)$ measurement reveal a predominant role of electrical heat conduction in the NiCo, NiFe, and NiCoFe alloys, while both electrons and phonons contribute to the total thermal conductivity in HEAs containing Cr/Mn/Pd. Overall, our results indicate a significant increase in chemical disorder, lattice defects, and lattice distortion in NiCo, NiFe, and NiCoFe with Cr/Mn/Pd alloying, which significantly affects the physical properties of the studied HEAs.

II. EXPERIMENTAL

The midperiod 3*d* and 4*d* transition metal-based HEAs of binary, ternary, quaternary, and quinary alloys, including NiCo, NiFe, NiCoFe, NiCoMn, NiCoCr, NiFeMn, NiCoFeMn, NiCoFeCr, NiCoMnCr, NiCoFeMnCr, and NiCoFeCrPd, were prepared using an arc-melting method under an argon atmosphere by taking the stoichiometric amount of the high-purity Ni, Co, Fe, Cr, Mn, and Pd elements. The ingots were flipped and remelted several times in the arc furnace to obtain a better compositional homogeneity. A Ti ball was melted before each melting to absorb residual oxygen in the arc-furnace chamber. The weight loss during melting was <0.1%. The as-cast samples were then homogenized at 1100–1200 °C for 24 h followed by water quenching. The homogenized ingots were further cold-rolled at room temperature to a plate of ~2 mm thickness by the thickness reduction of 0.2–0.3 mm for each rolling.

The phase purity and crystallographic structure of the homogenized polycrystalline samples were analyzed by employing the XRD measurement on the polished surface of the ingot at room temperature using Cu K_α radiation ($\lambda = 1.5418$ Å; 2θ ranges from 20° to 80° with a step size of 0.02°) on a commercial diffractometer. The XRD data have been analyzed using the Le Bail fit with FULLPROF suite software package and confirmed that all HEAs in this paper were in single-phase Cu-type fcc structure [43]. The polished samples were further examined in a field-emission scanning electron microscope (FESEM, NOVA NANO 450 model, Oregon, USA) in the backscattered electron mode. A commercial Vickers microhardness instrument (Mitutoyo HM, Japan) was used to measure the Vickers hardness (Hv) with an applied load of 300 g and a loading time of 15 s. The hardness values were averaged from at least eight data for each specimen. The electrical resistivity was performed using the standard four-probe direct current method in the temperature range 10–300 K by a closed-cycle refrigerator. The Seebeck coefficient and thermal conductivity measurements were carried out simultaneously in a home-built apparatus using a direct heat pulse technique. These electrical and thermal transport measurements were carried out on parallelepiped-shaped samples of dimensions of $\sim 5.0 \times 1.5 \times 1.5\ \text{mm}^3$. The details of these measurements can be found elsewhere [44].

III. RESULTS AND DISCUSSIONS

A. Phase analysis, microstructure, and hardness

Figure 1 represents the XRD patterns collected at room temperature of the equiatomic HEAs, including NiCoMn, NiFeMn, NiCoFeMn, NiCoCr, NiCoFeCr, NiCoMnCr, NiCoFeMnCr, and NiCoFeCrPd. All XRD patterns of the

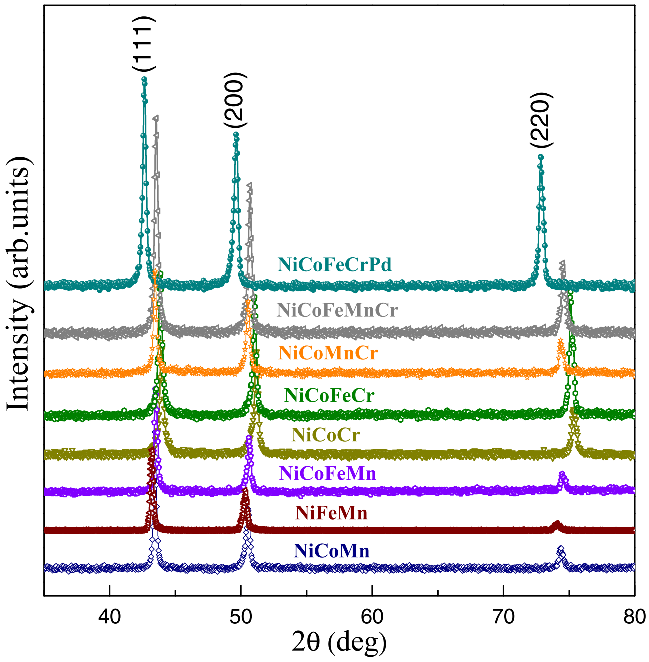

FIG. 1. Room-temperature x-ray diffraction (XRD) patterns of the cold-rolled NiCoMn, NiFeMn, NiCoFeMn, NiCoCr, NiCoFeCr, NiCoMnCr, NiCoFeMnCr, and NiCoFeCrPd alloys.

studied samples appear to be nearly identical, and the diffraction peaks could be indexed by the simple Cu-type fcc crystal structure with space group Fm-3m. The lattice constant (a) of the fcc phase for all alloys was obtained using the Le Bail fit and summarized in Table I [43]. In Table I, we have also listed the lattice constants of the NiCo, NiFe, and NiCoFe alloys from the previous report for comparison [20]. It can be seen that, with alloying of NiCo, NiFe, and NiCoFe with Mn, Cr, and Pd, the lattice constants of the NiCoMn, NiFeMn, NiCoFeCr, NiCoFeMn, NiCoCr, NiCoMnCr, NiCoFeMnCr, and NiCoFeCrPd alloys show a somewhat larger value than those of the NiCo, NiFe, and NiCoFe alloys because Pd, Cr, and Mn have larger atomic radii than that of the Ni, Co, and Fe. Further, the valence electron concentration (VEC), i.e., the number of the valence electrons per formula unit of the constituents in the alloys, including d electrons, is also calculated using Ref. [45] and listed in Table I. The obtained VEC values are consistent with the prediction by Guo *et al.* [45,46], in which HEAs formed a single-phase fcc structure when the effective VEC of an alloy was >8.

Since the atomic size of constituents (Ni, Co, Fe, Mn, Cr, and Pd) in the present HEAs lies between 150 and 170 pm, therefore, during solidification, each element can be expected to be distributed homogeneously and randomly at different lattice sites of the fcc unit cell with no long-range compositional order. However, there could exist short-range order in these alloys. This degree of disorder leads to a local chemically disordered and complex environment, which can produce several site-to-site lattice distortions in the lattice. Such an observation is found to be fundamentally different from pure metals and chemically ordered intermetallic alloys. To investigate this speculation, the lattice distortion was evaluated in all equiatomic HEAs with respect to the Ni lattice, which is defined as $\zeta = (a_{\mathrm{EEA}} - a_{\mathrm{Ni}})/a_{\mathrm{Ni}}$ [46]. Here, a_{EEA} and a_{Ni} are the lattice constants for the equiatomic alloys and pure Ni, respectively. The calculated values of lattice distortion of all alloys are tabulated in Table I using $a_{\mathrm{Ni}} = 3.524$ Å [46]. It is noticed that the lattice distortion in the Pd-containing quinary NiCoFeCrPd alloy is about twice as high as the other alloys, most likely due to a different lattice symmetry or geometry and synergetic effect of chemical complexity [47]. This finding agrees with the reported synchrotron XRD results, where the atomic size mismatch of the constituent elements was reported to be larger [47,48].

To investigate the microstructures of the studied HEAs, the SEM images were taken on the polished surfaces at room temperature. Figures 2(a)–2(d) show the typical low magnification backscattered electron (BSE) images for representative Cr/Mn/Pd-containing alloys, e.g., NiCoCr, NiCoMnCr, NiCoFeMnCr, and NiCoFeCrPd. The BSE images of these cold-rolled HEAs indicate that all alloys are essentially single-phase fcc solid solutions, with the inclusion of small dark spots. The dark spots are oxide particles resulting from the residual oxygen in the raw materials and/or possibly from oxidation during arc melting. Because of their tiny volume fractions, they do not influence the studied physical properties, as shown below. As one can see in Figs. 2(a)–2(d), the microstructures of all samples form large elongated grains along the rolling direction with lots of shear bands

TABLE I. Lattice constant, valence electron concentration (VEC), lattice distortion, microhardness, residual resistivity ratio (RRR), temperature coefficient of resistivity (TCR), and Curie temperature (T_C) [30,35,37,41,59] of the high-entropy alloys.

Sample	Lattice constant a (Å)	VEC	Lattice distortion (ζ)	Hardness (Hv)	RRR	TCR (10^{-4}/K)	T_C (K)
NiCo	3.534	9.50	0.0028	90.4 ± 3.9	3.66	30.40	1117
NiFe	3.583	9.00	0.0167	129.0 ± 4.8	3.34	34.80	780
NiCoFe	3.569	8.98	0.0128	121.7 ± 3.9	1.87	23.57	995
NiCoMn	3.614	8.66	0.0255	136.5 ± 1.6	1.08	4.62	–
NiFeMn	3.622	8.32	0.0278	128.6 ± 2.3	1.02	5.00	43
NiCoFeMn	3.593	8.50	0.0196	121.9 ± 2.4	1.06	3.49	156
NiCoCr	3.560	8.33	0.0102	158.0 ± 4.9	1.15	6.18	~0
NiCoFeCr	3.570	8.25	0.0131	133.6 ± 2.5	1.20	5.86	130
NiCoMnCr	3.599	8.00	0.0213	164.2 ± 4.9	1.07	4.78	–
NiCoFeMnCr	3.593	8.00	0.0196	136.1 ± 4.2	1.10	4.27	40
NiCoFeCrPd	3.669	8.60	0.0412	205.6 ± 2.1	1.06	4.37	440

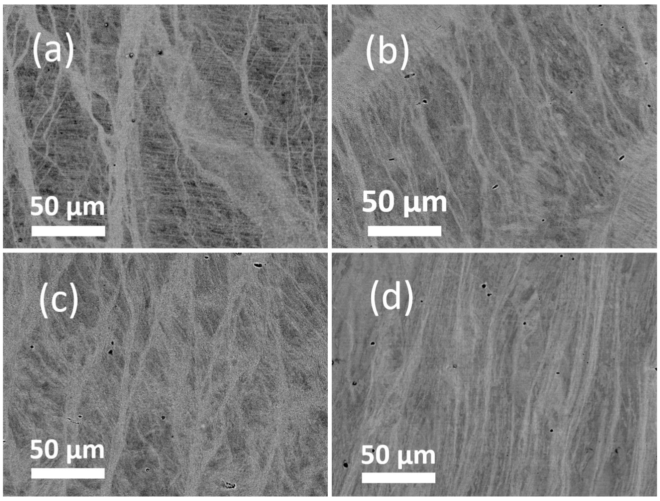

FIG. 2. Scanning electron microscopy (SEM) backscattered electron images of the polished surface of cold-rolled (a) NiCoCr, (b) NiCoMnCr, (c) NiCoFeMnCr, and (d) NiCoFeCrPd alloys.

and dislocations. Moreover, with increasing the number of elements in HEAs, the stretched-type grain areas are found to be increased. For the NiCoFeCrPd alloy, a dense elongated grained structure was found. These microstructural features were found to be related to the hardness of the materials, which will be discussed later. The microstructural features observed in this paper are like the previous reports on Ni-based HEAs [1]. We also observed deformation twins (twin boundaries) and textures in their microstructures, commonly found in recrystallized fcc metals and solid solutions. For example, Tsai *et al.* [49] found that nanotwins occurred in the early stage of cold-rolling in fcc-structured $Al_{0.5}$CoCrCuFeNi HEA because it has low stacking fault energy and high matrix strength. Additionally, Bhattacharjee *et al.* [50] found that fcc-structured CoCrFeMnNi HEA developed a predominantly brass-type texture and a submicron cell structure characterized by the presence of dense shear bands after heavy cold rolling. It indicates that the present fcc-structured HEAs have a low stacking fault energy.

To evaluate potential mechanical applications in the studied HEAs, microhardness was measured at room temperature. Table I summarizes the Hv values for all studied HEAs. It is found that the hardness values of the studied HEAs vary nonmonotonically with increasing the number of alloying elements. For the binary NiCo and NiFe alloys, the hardness is ∼90 and 129 Hv, respectively, while the ternary NiCoFe, NiCoMn, NiFeMn, and NiCoCr alloys show the hardness values of ∼121.7, 136.5, 128.6, and 158.0 Hv, respectively. Further, the hardness values of the quaternary NiCoFeMn, NiCoFeCr, and NiCoMnCr alloys are found to ∼121.9, 133.6, and 164.2 Hv, respectively, while the hardness values of the quinary NiCoFeMnCr and NiCoFeCrPd alloys are ∼136.1 and 205.6 Hv, respectively. This finding indicates that the hardness of the Cr- and Pd-containing HEAs is greater than the Mn-containing alloys and is consistent with the results reported by Wu *et al.* [1]. The higher hardness in the Cr-containing alloys was described by the higher Young's modulus of Cr atoms than that of Mn element. However, other factors such as atomic size mismatch, short-range ordering, chemical complexity, and stacking fault energy can also play some role in these HEAs [1,27]. The maximum hardness value (∼205 Hv) in the NiCoFeCrPd alloy is higher than certain austenitic stainless steels (∼193 Hv) and lower than martensitic stainless steels (∼330 Hv), commonly used for low-temperature purposes [51,52]. It suggests that the simple fcc-structured HEAs possess moderate mechanical properties, and further tuning could lead to potentially cryogenic and industrial applications.

B. Electrical resistivity

The temperature-dependent electrical resistivity $\rho(T)$ of all investigated HEAs, over the temperature range $10\,\mathrm{K} \leqslant T \leqslant 300\,\mathrm{K}$, normalized with respect to the resistivity at 10 K [i.e., $r(T) = \rho(T)/\rho_{10\,\mathrm{K}}$, where $\rho_{10\,\mathrm{K}}$ is the electrical resistivity at 10 K], is presented in Fig. 3. Figure 3(a) displays the normalized resistivity $r(T)$ of the NiCo, NiFe, and NiCoFe alloys. It is seen that these alloys exhibit a positive temperature coefficient of resistivity (TCR), $1/\rho d\rho/dT$, over the entire temperature range, indicating metallike electrical conduction [23,24]. The residual resistivity at 10 K ($\rho_{10\,\mathrm{K}}$) in these alloys is observed to be in the range of ∼2–13 $\mu\Omega$-cm, comparable with those of elemental metals. These values agree well with the earlier reports and indicate that the electron scattering in these alloys is weakly affected by chemical disorders and lattice defects such as vacancies, dislocations, imperfections, and stacking faults [25,26,29]. Furthermore, the low resistivity value in these alloys may result from the majority magnetic-spin channel alignment, which reduces the scattering of conduction electrons [25]. The values of $r(T)$ at 300 K, i.e., the residual resistivity ratio (RRR $= \rho_{300\,\mathrm{K}}/\rho_{10\,\mathrm{K}}$) for these alloys, range from 2 to 4.

Figures 3(b) and 3(c) illustrate the $r(T)$ of the Mn-containing alloys (NiCoMn, NiFeMn, and NiCoFeMn) and the Cr-containing alloys (NiCoCr and NiCoFeCr), respectively. It is noted that the values of $\rho_{10\,\mathrm{K}}$ for these Cr/Mn-containing alloys are much higher ($\geqslant 70$ $\mu\Omega$-cm) than the NiCo, NiFe, and NiCoFe alloys, implying an increase in electron scattering with the chemical disorders, lattice defects, and lattice distortion in these alloys. However, no correlation with the number of alloying elements in HEAs could be found because all elements were distributed randomly in the lattice. The highest $\rho_{10\,\mathrm{K}}$ value is observed to be ∼135 $\mu\Omega$-cm for the NiFeMn alloy. The higher value of ρ is consistent with the decreased VEC values of these alloys with Cr/Mn element (see Table I), indicating the Fermi energy (E_F) level is expected to move closer to the valence band, and the E_F falls near the high density of states (DOS) *d* bands [25]. We also found that the RRR values for these Cr/Mn-containing alloys are in the range from 1.02 to 1.20. This reflects the broadening of the Fermi energy, as seen in the electronic band structure in the NiCoFeCr alloy [25,53]. In addition, a magnetic disorder due to complex AFM ground states of the Cr and Mn elements could also influence the electrical resistivity, as both spin channels experience strong disorder scattering due to the electron filling effect [54]. It is noted that the ρ values in these alloys are between that of the conventional alloys such as stainless steel, low carbon steel, and Ni steel [55], and that of

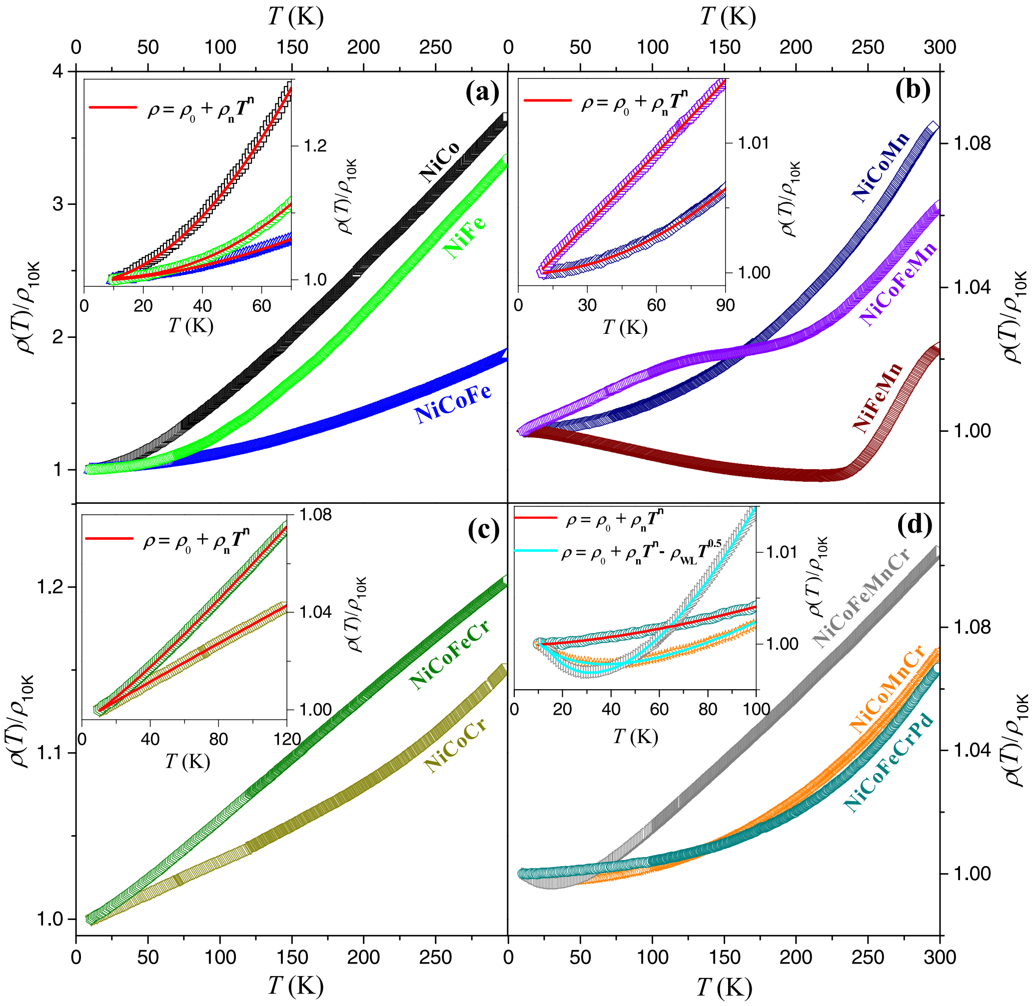

FIG. 3. Temperature-dependent normalized electrical resistivity with respect to the resistivity at 10 K $\rho_{10\,K}$ (i.e., $\rho(T)/\rho_{10\,K}$) for the (a) NiCo, NiFe, NiCoFe, (b) NiCoMn, NiFeMn, NiCoFeMn, (c) NiCoCr, NiCoFeCr, (d) NiCoMnCr, NiCoFeMnCr, and NiCoFeCrPd alloys. Insets highlight the low-temperature $\rho(T)/\rho_{10\,K}$ data, and the solid line represents the fit using the power law and weak localization effect.

the bulk metallic glasses or amorphous alloys, such as Ni-Zr, Co-Zr, Ni-Pt-P, and Ni-Zr-Ti [56–58], suggesting that these highly resistive Cr/Mn-containing alloys could be useful for the production of high-quality resistors.

It is seen in Figs. 3(b) and 3(c) that the characteristics of $r(T)$ change drastically for the Mn/Cr-containing alloys. Upon heating, the NiCoMn, NiCoCr, and NiCoFeCr samples show metallic behavior over the measured temperature range. In Table I, we have listed the magnetic transition temperatures (T_C) of all alloys taken from Refs. [30,35,37,41,59]. No distinct sign of the magnetic transition of NiCoFeCr in $r(T)$ is observed, while the $r(T)$ of the NiCoFeMn sample shows a plateaulike feature near the Curie temperature [41]. Presumably, a reconstruction of the Fermi surface occurs at the transition in the NiCoFeMn alloy. The $r(T)$ of the NiFeMn alloy exhibits a negative TCR <230 K with $r \simeq 0.98$, like that of the amorphous or disordered alloys [58,60]. For $T > 230$ K, the $r(T)$ increases sharply with the TCR $\simeq 5.0 \times 10^{-4}$/K and $\rho \simeq 138\ \mu\Omega$-cm at 300 K. The magnetic state of the NiFeMn alloy is unknown; however, it has been theoretically predicted that its Curie temperature is ~43 K [59]. Therefore, the positive TCR in $r(T)$ at high temperatures indicates a considerable modification of the electronic band structure near the Fermi surface [53]. It has been suggested theoretically that the noncollinear/disordered local magnetic moment of the Mn moment is more favorable at low temperatures than the AFM state in the NiCoMn alloy [33]. Therefore, a possible reason for such a change in the electronic structure in the NiFeMn sample ~230 K is due to the coexisting of two types of magnetic states of Mn.

The variation of $r(T)$ for the NiCoMnCr and NiCoFeMnCr alloys containing both Mn and Cr is shown in Fig. 3(d). Upon cooling, the $r(T)$ of NiCoFeMnCr and NiCoMnCr alloys decreases gradually and develops a distinct minimum near $T_m \approx 30$ and 40 K, respectively [see the inset of Fig. 3(d)], followed by an upturn below T_m with $\rho_{10\,K}$ values on the order of $10^2\ \mu\Omega$-cm. The large residual resistivity indicates their strongly defective fcc crystal structure and disordered lattice. The negative TCR feature at low temperatures in these highly resistive HEAs is like that observed in many ternary and quaternary Heusler alloys (e.g., $Co_2Fe_{0.5}Cr_{0.5}Si$ and CoFeMnGe) [61,62] and dilute crystalline alloys (e.g., $Ni_{1-x}Fe_xCr$ and $Co_{1-x}Al_x$), [23,24,63] and is typically attributed to the disorder-induced coherent backscattering of conduction

TABLE II. Temperature dependence of electrical resistivity in the low-T region, which is fitted by the equation $\rho = \rho_0 + \rho_n T^n - \rho_{\mathrm{WL}} T^{0.5}$.

Sample	ρ_0 ($\mu\Omega$ cm)	$\rho_n T^n$ (10^{-3} $\mu\Omega$ cm)	$\rho_{\mathrm{WL}} T^{0.5}$ ($\mu\Omega$ cm)	Temperature range fitted (K)
NiCo	2.87	$0.24T^{1.92}$	–	<75
NiFe	12.33	$0.05T^{2.40}$	–	<75
NiCoFe	12.73	$0.30T^{1.85}$	–	<75
NiCoMn	91.36	$0.07T^{2.0}$	–	<120
NiCoFeMn	93.26	$14.06T^{1.04}$	–	<90
NiCoCr	79.69	$33.6T^{0.98}$	–	<120
NiCoFeCr	69.24	$26.4T^{1.12}$	–	<120
NiCoMnCr	104.20	$5.2T^{1.28}$	$0.23T^{0.5}$	<120
NiCoFeMnCr	89.81	$6.8T^{1.40}$	$0.43T^{0.5}$	<100
NiCoFeCrPd	90.77	$0.20T^{1.65}$	–	<100

electrons, a mechanism known as weak localization effect induced by chemical disorder [64]. The $r(T)$ of alloying NiCoFeCr with Pd (NiCoFeCrPd), on the other hand, shows metallic characteristics over the studied temperature range with no minimum down to 10 K, and the value of $\rho_{10\,\mathrm{K}}$ is ~91 $\mu\Omega$-cm. This observation is consistent with the earlier report that the minimum feature in $\rho(T)$ is much less significant in the NiCoFeCrPd alloy [26]. The possible reason for the observation may be connected to the increased inelastic scattering of conduction electrons of the Pd in the NiCoFeCrPd sample with the phonons and magnons, which could suppress the minimum in electrical resistivity at low temperatures [26,37]. The relatively small RRR values in these alloys (see Table I) suggest a large concentration of chemical disorders and defects in the Cr/Mn/Pd-containing alloys.

It is noted that the $\rho(T)$ data of all investigated alloys show a monotonic variation with the temperature at high temperatures. We calculated the TCR for $T > 200$ K by the relation as $(\rho_{300\,\mathrm{K}} - \rho_{200\,\mathrm{K}})/(\rho_{300\,\mathrm{K}})$, where $\rho_{200\,\mathrm{K}}$ and $\rho_{300\,\mathrm{K}}$ are the electrical resistivities at 200 and 300 K, respectively. The calculated TCR values listed in Table I indicate that the NiCoMn, NiCoFeMn, NiCoCr, NiCoFeCr, NiCoMnCr, NiCoFeMnCr, and NiCoFeCrPd alloys have a lower TCR value of ~ 3.7–5.9×10^{-4}/K, while a higher TCR value for the NiCo, NiFe, and NiCoFe alloys in the range from 23.6 to 30.4×10^{-4}/K is found. The larger values of TCR in NiCo, NiFe, and NiCoFe alloys is most likely due to an increased electron scattering by magnons, as T_C for these alloys is $\gg$300 K. Moreover, these TCR values are comparable with the various conventional alloys such as Al-Mg, Cu-Zn, Fe-Ni, and stainless steels [26,27,31]. On the other hand, the lower values of TCR in Cr/Mn/Pd-containing HEAs can be explained by the weaker lattice vibration associated with a higher rigidity due to their enhanced lattice distortion and compositional complexity. The lowest TCR values in these highly resistive alloys can be related to the MIR limit for a crystalline solid, e.g., NiCr, MnPd, NiCu, and FeCr [23,24,65,66], where the electron mean free path reaches their interatomic spacing.

To unveil the conduction mechanisms involved in $\rho(T)$ at low temperatures in their crystal lattice of the studied HEAs, we have attempted various functional forms. We found that the $\rho(T)$ data of these samples can be satisfactorily fitted by a general power-law equation $\rho(T) = \rho_0 + \rho_n T^n$ (where ρ_0 is the residual resistivity, and ρ_n and n are fitting parameters). The fitting parameters and the temperature range for the fit are summarized in Table II, and the resultant fits are represented by the solid lines in Fig. 3. The best fit of $\rho(T)$ data for the NiCo and NiCoFe samples yields $n \simeq 1.92$ and 1.85, respectively, while the fit for the NiFe sample yields a relatively higher $n \simeq 2.40$. In these studied alloys, like conventional alloys, the scattering takes place by both localized and itinerant electrons. In the case of alloys that contain transition metals, the electron-phonon interaction ($\rho_{e\text{-}p}$) generally takes place from the s-d scattering at low temperatures, and $\rho(T)$ can be described by $n = 3$ rather than the usual $n = 5$ in the Bloch-Grunessen formula for a simple metal [67]. In addition, electron-electron scattering ($\rho_{e\text{-}e}$) follows a T^2 dependence on ρ at low temperatures in the metallic alloys. Furthermore, as the FM Curie temperature of these metallic samples is reported to be $\gg$300 K (see Table I), therefore a T^2 dependence of ρ due to electron-magnon scattering ($\rho_{e\text{-}m}$) also plays a role in the $\rho(T)$ at low temperatures [24,29]. The obtained value of n in the NiFe alloy falls in between 2 and 3, suggesting a combination of the $\rho_{e\text{-}e}$, $\rho_{e\text{-}p}$, and $\rho_{e\text{-}m}$ contributions in $\rho(T)$. In contrast, the values of n in the NiCo and NiCoFe alloys are close to $n = 2$, indicating the predominant contribution of $\rho_{e\text{-}e}$ and $\rho_{e\text{-}m}$ at low temperatures. However, it is difficult to differentiate each scattering term from the present simple analysis.

The fit of the NiCoMn sample also gives $n \simeq 2.0$. Further, the fitting of NiCoFeMn, NiCoCr, and NiCoFeCr data yields $n \simeq 1.04$, 0.98, and 1.12, respectively, close to $n = 1$, suggesting a dominant direct electron-phonon scattering contribution in $\rho(T)$. Nearly linear T dependence of ρ at low temperatures is in agreement with the theoretical prediction of some transition metal-based alloys such as NiCoCr, $\mathrm{Fe_3GeTe_2}$, and $\mathrm{Ir_3Te_8}$, where the residual resistivity falls near or above the MIR limit [68–70]. It implies that the diffusive transport behavior dominates the electrical transport in NiCoFeMn and NiCoFeCr alloys, and these alloys can be classified as dirty or poor metal [68,71].

We now discuss the low-T $\rho(T)$ data of NiCoMnCr and NiCoFeMnCr alloys [see Fig. 3(d)]. As we already discussed, the resistivity minimum at low temperatures in these two HEAs can be explained by the disorder-aided enhancement in electron-electron interaction due to diffusive electrons motion [64]. It has been noted that Jin *et al.* [26] interpreted this minimum in the NiCoFeMnCr sample by the Kondo effect due to coupling between the conduction electrons and localized magnetic impurities. However, we expect that the localization

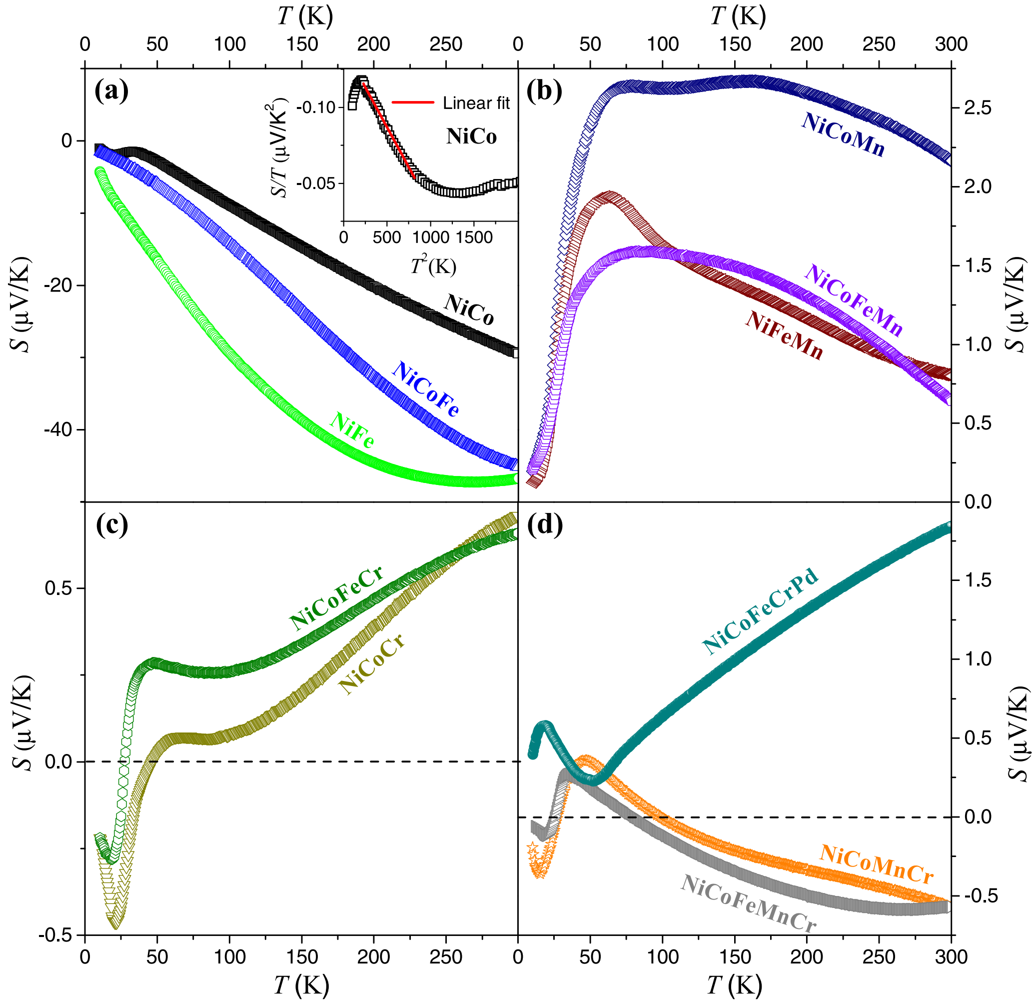

FIG. 4. Temperature-dependent Seebeck coefficient $S(T)$ of the high-entropy alloys for (a) NiCo, NiFe, NiCoFe, (b) NiCoMn, NiFeMn, NiCoFeMn, (c) NiCoCr, NiCoFeCr, (d) NiCoMnCr, NiCoFeMnCr, and NiCoFeCrPd. Inset shows the S/T vs T^2 plots in the low-temperature regime for the NiCo alloy. The solid line represents the linear fit at low temperatures.

effect is applicable in this paper, as the residual resistivity of these samples is on the order of 10^2 $\mu\Omega$ cm, and the $\Delta\rho/\rho_{300\,\mathrm{K}}$ is in the range of 7–10%, where $\Delta\rho = \rho_{300\,\mathrm{K}} - \rho_{\mathrm{min}}$ (ρ_{min} is the resistivity value at T_m). Additionally, the variation of resistivity at low temperatures below T_m is <0.5%. Therefore, we added a weak localization effect ($\rho_{\mathrm{WL}} \approx -T^{0.5}$) term to the power-law equation, which is independent of the magnetic states of the alloys. From the fitting, we obtained $n \simeq 1.30$ and 1.40 for the NiCoMnCr and NiCoFeMnCr samples, respectively, as shown in Table II. For the NiCoFeCrPd sample, the low-T $\rho(T)$ data is fitted using only the power-law equation and yields $n \simeq 1.65$. It appears that the obtained exponent n for these Cr/Mn/Pd-containing samples lies between 1 and 2, like that observed in many half-metallic FM Heusler alloys, such as Co_2FeSi, CoRuFeGe, and CoRhMnFe [72–74], providing possible evidence of half-metallic nature in these alloys.

C. Seebeck coefficient

To understand the nature of charge carriers near the Fermi surface in the studied HEAs, the Seebeck coefficient $S(T)$ was measured as a function of temperature, as shown in Fig. 4. The Seebeck coefficient is a sensitive probe that can provide complementary information about the electronic band structure near the Fermi level and the change in the position of Fermi energy of a material. Figure 4(a) shows negative $S(T)$ values for the NiCo, NiFe, and NiCoFe alloys, indicating that the electron-type carriers dominate the thermoelectric transport, as the pure Ni element [75]. At 300 K, the magnitude of S ($S_{300\,\mathrm{K}}$) is ~30 μV/K for the NiCo sample, whereas $S_{300\,\mathrm{K}}$ is increased to ~45 and 47 μV/K for the NiCoFe and NiFe samples, respectively, indicating a change in the carrier scattering with Fe alloying. These S values are considerably higher than the elemental metals [75] and some *3d* transition metal-based intermetallic alloys (e.g., Ni_3Co, $Al_{13}Co_4$, and $MoTe_2$) [76–78] and the Heusler alloys (e.g., Ni_2MnGa, Fe_2VAl, and Co_2TiSi) [79–81].

A quasilinear $S(T)$ feature at high temperatures in the NiCo alloy suggests a metallic diffusionlike thermoelectric transport. However, there could be some magnetic contribution in these alloys due to the electron-magnon interaction. Overall, the $S(T)$ behavior is like that found in pure Ni [75]. As the magnitude of S of a metallic sample depends on the position of

E_F in electronic DOS, therefore, we have calculated the Fermi energy (E_F) of the NiCo sample from the $S(T)$ data using the Mott formula ($S = \pi^2 k_B{}^2 T/2eE_F$, where k_B is the Boltzmann constant, and e is the elementary charge) for ordinary metals, assuming a single-band model with an energy-independent relaxation time. The obtained $E_F \simeq 0.38\,\mathrm{eV}$ for the NiCo is comparable with that of Ni, indicating the metallic nature of NiCo. However, for NiFe and NiCoFe, the $S(T)$ is not linear and shows a tendency to saturate near room temperature. It has been shown that pure Fe shows a magnon-drag effect ~200 K due to the electron-magnon interaction [75]. Therefore, the nonlinearity at high temperatures in NiFe and NiCoFe samples could be related to the magnon-drag effect of Fe. For the NiCoFe sample, a linear $S(T)$ behavior is seen at the intermediate temperatures for the $T = 100$–$250\,\mathrm{K}$ range and fitted by the Mott formula. The obtained $E_F \simeq 0.20\,\mathrm{eV}$ is slightly smaller than for the NiCo alloy. It indicates that the observed variation in the magnitude of S ~300 K in the NiFe and NiCoFe alloys is related to a shift in the position of E_F with incorporating Fe. By contrast, at low temperatures, a peaklike feature ~30 K in the NiCo alloy is observed; however, no such feature can be seen in the NiFe and NiCoFe alloys. The peaklike behavior in S at low temperatures is often associated with the electron-phonon effect, which generally varies as T^3 in the phonon-drag model. Also, the temperature of this peak for NiCo occurs below the $\theta_D/10$ (θ_D is the Debye temperature) limit [82]. In the inset of Fig. 4(a), we plotted S/T vs T^2 for the NiCo sample. The nearly linear behavior indicates a phonon-drag mechanism for the peaklike feature at low temperatures [44,80]. Further, it is well known that the disorder/impurities in a conventional metal could suppress the phonon-drag feature, indicating that the NiCo sample might be more ordered than the NiFe and NiCoFe samples.

Figures 4(b)–4(d) show the $S(T)$ data of the HEAs containing Mn, Cr, and both Mn and Cr, respectively. The value of S for all studied alloys tends toward zero as T approaches zero, indicating the diffusive contribution of S. With increasing temperature, the S of these alloys showed a nonmonotonic behavior with temperature. We note that the absolute value of S in these alloys is ~0.5–2.5 μV/K at 300 K, much smaller than that of the NiCo, NiFe, and NiCoFe alloys, suggesting the divergence of electronic bands. Such a range of S value is generally observed in amorphous or disordered alloys and quasicrystals, e.g., Mg-Zn, Cu-Zr-Ti, Ti-Zr-Ni, and Ag-In-Yb. [58,60,83,84]. Additionally, the small S values are also observed in some HEAs, such as Al_xCoCrFeNi and CoCrFeNiNb$_x$ [7,85]. It indicates that Mn/Cr elements produce a large amount of structural and magnetic disorders in the alloys that contribute to additional electron scattering, which in turn results in a small value of S. In addition, the local atomic structure of Cr and Mn in HEAs with fcc structure plays an essential role in electrical transport. For example, Zhang *et al.* [21] proposed that Cr atoms are favorably bonded with Ni and Co rather than other Cr atoms in the NiCoCr alloy and may form a short-range order due to their chemical complexity, leading to the low values of the S.

Figure 4(b) shows that the S values of the Mn-containing NiCoMn, NiFeMn, and NiCoFeMn alloys are positive in the entire temperature range under investigation. The sign reversal of the charge carriers from electrons to holes with alloying Mn in the NiCo, NiFe, and NiCoFe alloys indicates a substantial change in the electronic band structure or conduction mechanism of the dominant carrier [25]. As the VEC of the Mn is lower than Ni, Co, and Fe, Mn in these alloys could cause a substantial downward shift of E_F, resulting in a reduction of electron concentrations. Also, the band broadening/narrowing via changes in the unit cell volume, the chemical disorder, and spin-mixing with Mn alloying could modify the electronic DOS near E_F. With increasing temperature, the $S(T)$ of these alloys increases monotonically due to an increased carrier degeneracy and reaches a broad maximum between 50 and 70 K, then slowly decreases in $S(T)$ at high temperatures. As the absolute value of S in these alloys is smaller (<2.5 μV/K), the size of the electron and hole pockets is expected to be comparable, and electron and hole carriers are nearly compensated. The feature of a maximum in $S(T)$ data suggests the coexistence of the heavier electron and the lighter hole in the electronic band structure [86,87].

On the other hand, the $S(T)$ of the Cr-containing alloys (NiCoCr and NiCoFeCr), shown in Fig. 4(c), exhibits a quasilinear behavior with positive S values at high temperatures, signifying the hole-type diffusion thermoelectric transport. The hole-type conduction in the Cr-containing alloys is consistent with a dominant hole-type response in the Hall measurement in Al_xCoCrFeNi HEAs [28]. With decreasing temperature, the $S(T)$ develops a broad maximum of ~40–60 K, and then S changes signs from positive to negative values at low temperatures. The sign reversal in S is presumably attributed to the negative phonon-drag effect, evidenced by the pronounced dips ~20 K for the Cr-containing samples. A similar feature of $S(T)$ can be observed in many intermetallic alloys (e.g., $\mathrm{PtSn_4}$, $\mathrm{Cr_3PN}$, and FeSn) [88–90] and metallic glasses (e.g., Ti-Zr-Ni) [58]. This negative phonon-drag effect at low temperatures is generally attributed to the exchange of momentum among the charge carriers and phonons in metals, where the phononic mean free path is large [91].

The $S(T)$ of HEAs containing both Mn and Cr is shown in Fig. 4(d). As one can see, the S of the NiCoMnCr and NiCoFeMnCr alloys shows a complicated behavior with temperature. At high temperatures, the values of S for the NiCoMnCr and NiCoFeMnCr samples are negative, indicating that electron-type carriers dominate the thermoelectric transport. On the other hand, the $S(T)$ value for the Pd-containing alloy NiCoFeCrPd remains positive in the temperature range investigated, suggesting the hole-type thermoelectric conduction. Upon cooling, the magnitude of S in each sample decreases quasilinearly with temperature, indicating a typical characteristic of metallic diffusion behavior. Most interestingly, at low temperatures, $S(T)$ for the NiCoMnCr and NiCoFeMnCr alloys undergoes a sign reversal from negative to positive at ~80 and 100 K, respectively, and changes sign again to negative ~20 K due to the phonon-drag effect. Similar observations have been found in many metallic and semimetallic alloys, e.g., $\mathrm{Fe_{1.85}Ni_{0.15}VAl}$ [92], $\mathrm{FeAl_2}$ [93], and CuTe [94]. Therefore, the sign reversal in $S(T)$ at ~80 and 100 K for the NiCoMnCr and NiCoFeMnCr alloys, respectively, indicates the multiple band effect and can be ascribed to the change in the carrier mobility of electrons and holes with temperature. On the other hand, the S of NiCoFeCrPd alloy remains positive throughout the temperature range

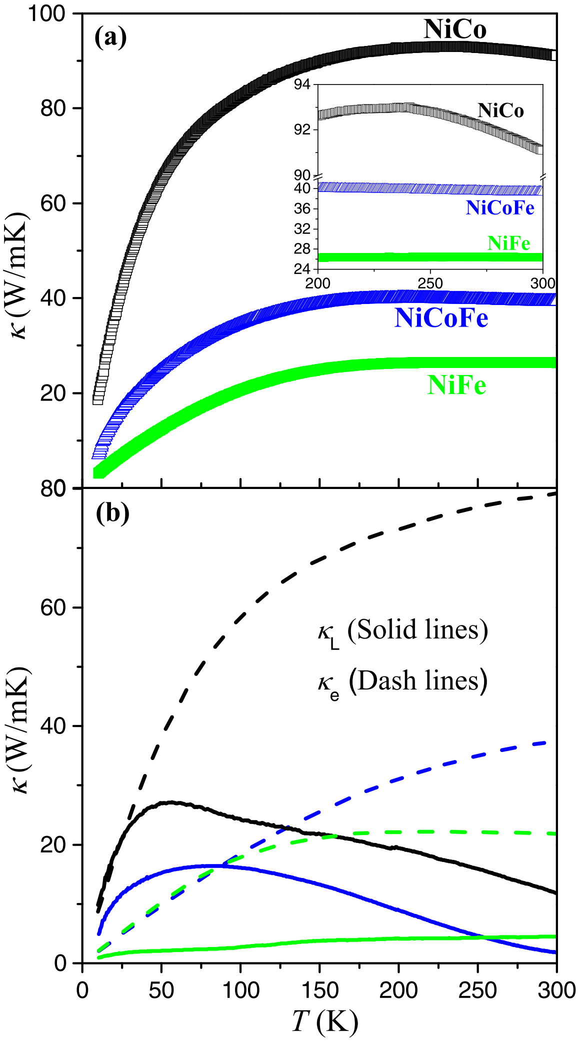

FIG. 5. (a) Temperature-dependent total thermal conductivity $\kappa(T)$ of the (a) NiCo, NiFe, and NiCoFe alloys. (b) Temperature-dependent lattice (κ_L) and electronic (κ_e) thermal conductivity of these alloys.

of investigation, suggesting higher mobility of holes than electrons. The positive value of S in the NiCoFeCrPd alloy can also be related to the variation of electronic DOS near E_F due to its large unit cell volume, disorder, and lattice distortion in the fcc unit cell.

D. Thermal conductivity

To understand the structural disorder in the present HEAs, the temperature-dependent thermal conductivity $\kappa(T)$ was measured over the temperature range 10–300 K. Figure 5(a) represents the behavior of $\kappa(T)$ of the NiCo, NiFe, and NiCoFe alloys, showing a similar temperature variation but different values of κ. The room-temperature κ value ($\kappa_{300\,\mathrm{K}}$) for the NiCo sample is quite large ~90 W/mK, while the $\kappa_{300\,\mathrm{K}}$ for the NiFe and NiCoFe samples is considerably smaller of ~22 and 37 W/mK, respectively. These κ values are found to be in good agreement with the literature [25,26,31]. The high κ in these metallic alloys could be desirable for high-temperature structural applications to enhance the heat transfer in the bulk samples, like many metals and alloys, e.g., Al, Ti, Pb, Cu, and Mg alloys [95]. Upon heating, the $\kappa(T)$ of these samples increases rapidly at low temperatures due to their growing excitation of heat carriers. In the temperature range of 100–225 K, the increase of $\kappa(T)$ slows down with temperature. As seen in the inset of Fig. 5(a), $\kappa(T)$ for NiCo and NiCoFe samples decreases slowly at high temperatures, like that observed by Samolyuk *et al.* [29], attributed to a decrease in the mean free path from the increased electron scattering by phonons and magnons.

In general, the total κ of a metal is the sum of two contributions from electrons (κ_e) and phonons (κ_L). As these alloys are FM in the investigated temperature range, the magnon contribution due to the interaction of magnetic moments with electrons and phonons may have a role in the measured κ. However, this contribution is expected to be very small as compared with the κ_e and κ_L, as observed in many magnetic alloys such as $\mathrm{Co_2Ti(Si/Ge/Sn)}$ and $\mathrm{UNi_{0.5}Sb_2}$ [81,96]. The κ_e in these alloys can be estimated using the Wiedemann-Franz law: $\kappa_e = L_0T/\rho$, where $L_0(=2.45 \times 10^{-8}\ \mathrm{W\Omega\ K^{-2}})$ is the Sommerfeld value of the Lorentz number. The Lorentz number in many cases of metals depends on the diffusion scattering mechanisms. In the present case, the $L(T)$ was determined by using the equation proposed by Kim *et al.* [97] $L = 1.5 + \exp(-|S|/116)$, where L is in the unit of $10^{-8}\ \Omega\mathrm{W\ K^{-2}}$ and S is in the unit of $\mu\mathrm{V/K}$. The obtained $\kappa_e(T)$ values using the T-dependent L and ρ values for the NiCo, NiFe, and NiCoFe alloys are plotted in Fig. 5(b). It appears that the κ_e increases monotonically with $T < 100$ K; then it shows a tendency of saturation. Such behavior is like that observed in many conventional metallic alloys [87,89,98,99], where the electronic heat conduction at low temperature is mainly dominated by the scattering of electrons with lattice defects and chemical disorders, while at high temperature, the scattering of electrons is mostly with phonons. A comparison of κ_e with the total κ indicates that the κ_e/κ ratio is ~87% for the NiCo sample, 83% for the NiFe sample, and 94% for the NiCoFe sample, suggesting a predominant role of κ_e in the heat conduction in these alloys. This observation is consistent with the metallic nature of these alloys that have a large κ_e, i.e., the heat conduction is predominantly carried by charge carriers rather than phonons. The temperature variation of κ_L obtained from the relation $\kappa(T) = \kappa_e(T) + \kappa_\mathrm{L}(T)$ is presented in Fig. 5(b). The room temperature κ_L for the NiCo, NiFe, and NiCoFe alloys is ~12, 4.5, and 2 W/m K, respectively. With decreasing temperature, the $\kappa_\mathrm{L}(T)$ for the NiCo and NiCoFe samples shows a broad humplike feature at ~50 and 75 K, respectively. Such a feature is like a typical κ_L vs T characteristic of crystalline solids or pure metals [99]. It is noted that the $\kappa_\mathrm{L}(T)$ of the NiFe alloy does not show a low-T hump; instead, it increases slowly with T, indicating the limitation of κ_L by point defects, static atomic disorders, and vacancies.

The $\kappa(T)$ of the Mn- and/or Cr-containing alloys are represented in Figs. 6(a)–6(c). Again, these alloys have a similar temperature dependence in $\kappa(T)$, except for a variation in the magnitude. Upon heating, the magnitude of κ for these alloys increases rapidly at low temperatures, and then it exhibits a quasilinear variation with T. Overall, this $\kappa(T)$ behavior is very similar to many half-metallic Heusler alloys (e.g.,

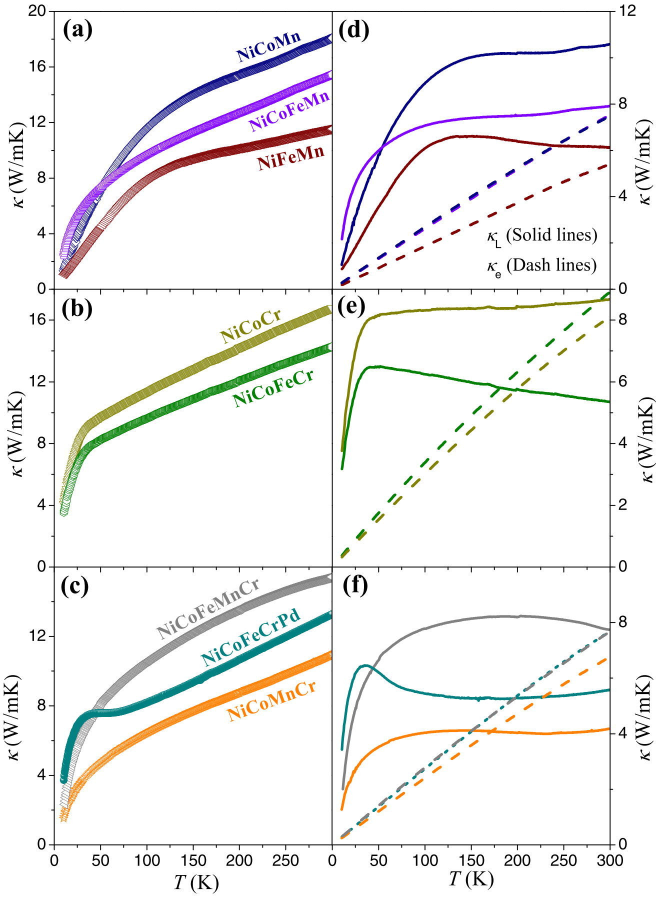

FIG. 6. Variation of total thermal conductivity $\kappa(T)$ for (a) NiCoMn, NiFeMn, NiCoFeMn, (b) NiCoCr, NiCoFeCr, (c) NiCoMnCr, NiCoFeMnCr, and NiCoFeCrPd alloys. Temperature-dependent lattice (κ_L) and electronic (κ_e) thermal conductivity of these high-entropy alloys are represented by solid and dash lines in (d), (e), and (f).

Co_2TiSi/Ge, Fe_2VAl, and Ru_2NbGa) [44,80,81] and the bulk metallic glasses (e.g., Cu-Zr-Ti and Ti-Zr-Ni) [58,60]. It is noted that the $\kappa(T)$ of the NiCoFeCrPd sample shows a broad peak or plateaulike feature at ~40 K [see Fig. 6(c)], which is one of the most prominent features for disordered solids.

The measured values of $\kappa_{300\,K}$ for these alloys are ~10–18 W/mK, much smaller than the NiCo, NiFe, and NiCoFe alloys. It is found that these κ values agree well with other HEAs, e.g., NiFeCrAl, CuCrFeTiV, AlCoCrFeNi, and $Ti_2NiCoSnSb$ [27,100–102]. Also, these κ values are comparable with those found in many disordered alloys and quasicrystals [58,60,83,103]. We calculated the κ_e and κ_L contributions, and the results are shown in Figs. 6(d)–6(f). The T-dependent κ_e shows a quasilinear variation over the investigated temperature range, consistent with the earlier results on the nonmagnetic NiCr and NiCoCr alloys [29] and some disordered alloys, e.g., CuZrNiTi and Ni_3AlC [104,105]. In all cases, it was speculated that the linear behavior in κ_e results from competition between κ reduction caused by electron-phonon scattering and T-induced increase in the number of heat carriers. At room temperature, the κ_e contributes ~40–60% of the total κ for these alloys. A similar findings in the $Al_xCoCrFeNi$, PbSnTeSe, and CuZrTiNi HEAs provide evidence for the semimetallic behavior in the Cr/Mn/Pd-containing alloys [27,105,106]. The significant reduction of κ_e in the Cr/Mn/Pd-containing alloys compared with the NiCo, NiFe, and NiCoFe alloys are mostly due to the extensive amount of chemical disorders/lattice defects/lattice-distortion in the fcc lattice, which act as scattering centers for electrons and lead to a considerable reduction of the electron mean free path [29,31]. Additionally, the electronic band-structure effect due to the Cr/Mn elements can reduce the κ_e, as elucidated theoretically for the NiCoFeCr alloy [25]. These observations resemble the high electrical resistivity and low VEC of the Cr/Mn/Pd-containing alloys.

The κ_L values at 300 K for the Cr/Mn-containing alloys are in the range of 5–11 W/mK [see Figs. 6(d)–6(f)], which lies in the same range for the NiCo, NiFe, and NiCoFe alloys [see Fig. 5(b)]. This observation suggests that the phonon scattering is comparable by incorporating Cr/Mn elements. It also indicates that the effect of scattering by alloying Cr/Mn elements is much stronger on the reduction of the mean free path of electrons than that of phonons. A similar low value of κ_L is also found in many half and full Heusler alloys such as NbFeSb, Ru_2NbGa, and Fe_2VGa [44,80,107]. Furthermore, the weak variation of $\kappa_L(T)$ in these Cr/Mn-containing HEAs indicates that the phonon scattering due to mass and size fluctuations is moderate, consistent with the little differences in microstructure in these alloys (see Fig. 2). The temperature variation of κ_L for these alloys in Figs. 6(d)–6(f) showed a slightly different behavior than the NiCo, NiFe, and NiCoFe alloys. In NiFeMn, NiCoFeCr, and NiCoFeCrPd samples, κ_L shows a broad peaklike feature at low temperatures, which is related to the reduction in phonon scatterings of solids. Additionally, it is found that the shape and position of the peak in κ_L varies for these alloys. For instance, the peak feature in the NiCoFeCrPd sample is more pronounced than NiFeMn and NiCoFeCr alloys. Further, for the NiFeMn sample, the peak appears at ~140 K, while the peak is at ~40 and 35 K for the NiCoFeCr and NiCoFeCrPd samples, respectively. The less point-defect scattering is likely to be the reason for the peak feature in these alloys. The earlier $\kappa(T)$ study in the NiCoFeCrMn and NiCoFeCrPd alloys show no low-T peak, suggesting that our present samples have fewer defects and are well ordered [26].

On the other hand, the obtained $\kappa_L(T)$ for the NiCoMn, NiCoFeMn, NiCoCr, NiCoCrMn, and NiCoFeCrMn alloys increases with increasing temperature, and the crystalline peak is suppressed, most probably due to the enhanced point-defect scattering in the local chemical disordered lattice. It increases smoothly and shows a tendency to saturate at high temperatures, presumably attributed to the activation of localized phonon states, as also observed in quasicrystals and disordered alloys [58,60,83,103]. Overall this $\kappa_L(T)$ feature is like the numerical calculation of κ_L in NiPd and NiPt alloys, indicating that the heat conduction is mainly mediated by long-wavelength phonon modes [108].

IV. CONCLUSIONS

In this paper, we investigated detailedly the physical properties of fcc-structured HEAs containing the midperiod 3d

transition metals Ni, Co, Fe, Mn, Cr, and 4*d* Pd. XRD results indicate a Cu-type cubic structure, and SEM images reveal elongated strained microstructures in these HEAs. The impact of the variation in these elements on the electrical and thermal transport properties was discussed. The electrical resistivity measurements show a metallic behavior in all investigated alloys; however, the residual resistivity, RRR, and TCR are varied significantly by alloying the Cr/Mn/Pd element. The temperature-dependent electron scattering mechanism at low temperatures was analyzed by the power-law equation. A nearly linear *T*-dependent resistivity in the NiCoCr, NiCoFeCr, and NiCoFeMn alloys was observed, presumably related to the MIR limit. In addition, the NiCoCrMn and NiCoFeCrMn alloys show a minimum in electrical resistivity, most likely due to a weak localization effect. These observations indicate a significant increase in disorder, lattice defects, and lattice distortion with alloying Cr/Mn/Pd. The Seebeck coefficient measurement indicated that the thermoelectric transport in NiCo, NiFe, and NiCoFe is governed by the electrons, while the hole-type carriers dominate in NiCoMn, NiFeMn, and NiCoFeMn alloys. A change in carrier types was found in the Cr-containing alloys, indicating multiband behavior. The Cr/Mn/Pd-containing HEAs show a lower *S* value, probably due to the compensation of carriers as the size of the electron and hole pockets are comparable in these alloys. The measured *T*-dependent thermal conductivity behaves similarly for all alloys, except for a significant reduction in magnitude in Cr/Mn/Pd-containing alloys. By separating the electronic and lattice contributions to the total thermal conductivity, predominant electronic contribution is found in alloys containing Ni, Co, and Fe, while electrons and lattice contribute near equally to the heat conduction in alloys containing Cr/Mn/Pd. The significant reduction in electronic thermal conductivity in the Cr/Mn/Pd-containing alloys is ascribed to the increased electron scattering by disorders and lattice distortions, as well as a substantial modification of band structure.

ACKNOWLEDGMENTS

This paper was supported by the Ministry of Science and Technology of Taiwan under Grant No. MOST-109-2112-M-259-007-MY3 (Y.-K.K.) and No. MOST-109-2221-E-002-120-MY2 (S.-K.W.).

---

[1] Z. Wu, H. Bei, F. Otto, G. M. Pharr, and E. P. George, Recovery, recrystallization, grain growth and phase stability of a family of fcc-structured multi-component equiatomic solid solution alloys, Intermetallics **46**, 131 (2014).

[2] W.-R. Wang, W.-L. Wang, and J.-W. Yeh, Phases, microstructure and mechanical properties of $Al_xCoCrFeNi$ high-entropy alloys at elevated temperatures, J. Alloys Compd. **589**, 143 (2014).

[3] B. Gludovatz, A. Hohenwarter, D. Catoor, E. H. Chang, E. P. George, and R. O. Ritchie, A fracture-resistant high-entropy alloy for cryogenic applications, Science **345**, 1153 (2014).

[4] Y. Zou, H. Ma, and R. Spolenak, Ultrastrong ductile and stable high-entropy alloys at small scales, Nat. Commun. **6**, 7748 (2015).

[5] M.-H. Chuang, M.-H. Tsai, W.-R. Wang, S.-J. Lin, and J.-W. Yeh, Microstructure and wear behavior of $Al_xCo_{1.5}CrFeNi_{1.5}Ti_y$ high-entropy alloys, Acta Mater. **59**, 6308 (2011).

[6] P. Kozelj, S. Vrtnik, A. Jelen, S. Jazbec, Z. Jaglicic, S. Maiti, M. Feuerbacher, W. Steurer, and J. Dolinsek, Discovery of a Superconducting High-Entropy Alloy, Phys. Rev. Lett. **113**, 107001 (2014).

[7] S. Shafeie, S. Guo, Q. Hu, H. Fahlquist, P. Erhart, and A. Palmqvist, High-entropy alloys as high-temperature thermoelectric materials, J. Appl. Phys. **118**, 184905 (2015).

[8] M. C. Gao, D. B. Miracle, D. Maurice, X. Yan, Y. Zhang, and J. A. Hawk, High-entropy functional materials, J. Mater. Res. **33**, 3138 (2018).

[9] R. Zhang, S. Zhao, J. Ding, Y. Chong, T. Jia, C. Ophus, M. Asta, R. O. Ritchie, and A. M. Minor, Short-range order and its impact on the CrCoNi medium-entropy alloy, Nature **581**, 283 (2020).

[10] L. J. Santodonato, Y. Zhang, M. Feygenson, C. M. Parish, M. C. Gao, R. J. K. Weber, J. C. Neuefeind, Z. Tang, and P. K. Liaw, Deviation from high-entropy configurations in the atomic distributions of a multi-principal-element alloy, Nat. Commun. **6**, 5964 (2015).

[11] Y. Zhang, T. Zuo, Y. Cheng, and P. K. Liaw, High-entropy alloys with high saturation magnetization, electrical resistivity and malleability, Sci. Rep. **3**, 1455 (2013).

[12] T. Osaka, M. Takai, K. Hayashi, K. Ohashi, M. Saito, and K. Yamada, A soft magnetic CoNiFe film with high saturation magnetic flux density and low coercivity, Nature **392**, 796 (1998).

[13] M. C. Gao, J.-W. Yeh, P. K. Liaw, and Y. Zhang, *High-entropy alloys: Fundamentals and applications* (Springer, New York, 2016).

[14] D. B. Miracle and O. N. Senkov, A critical review of high entropy alloys and related concepts, Acta Mater. **122**, 448 (2017).

[15] Y. Zhang, T. T. Zuo, Z. Tang, M. C. Gao, K. A. Dahmen, P. K. Liaw, and Z. P. Lu, Microstructures and properties of high-entropy alloys, Prog. Mater. Sci. **61**, 1 (2014).

[16] B. Cantor, I. Chang, P. Knight, and A. Vincent, Microstructural development in equiatomic multicomponent alloys, Mater. Sci. Eng. A **375**, 213 (2004).

[17] J.-W. Yeh, S.-K. Chen, S.-J. Lin, J.-Y. Gan, T.-S. Chin, T.-T. Shun, C.-H. Tsau, and S.-Y. Chang, Nanostructured high-entropy alloys with multiple principal elements: novel alloy design concepts and outcomes, Adv. Eng. Mater. **6**, 299 (2004).

[18] O. N. Senkov, J. D. Miller, D. B. Miracle, and C. Woodward, Accelerated exploration of multi-principal element alloys with solid solution phases, Nat. Commun. **6**, 6529 (2015).

[19] O. N. Senkov, G. Wilks, J. Scott, and D. B. Miracle, Mechanical properties of $Nb_{25}Mo_{25}Ta_{25}W_{25}$ and $V_{20}Nb_{20}Mo_{20}Ta_{20}W_{20}$ refractory high entropy alloys, Intermetallics **19**, 698 (2011).

[20] Z. Wu, M. C. Troparevsky, Y. Gao, J. R. Morris, G. M. Stocks, and H. Bei, Phase stability, physical properties and strengthening mechanisms of concentrated solid solution alloys, Curr. Opin. Solid State Mater. Sci. **21**, 267 (2017).

[21] F. Zhang, S. Zhao, K. Jin, H. Xue, G. Velisa, H. Bei, R. Huang, J. Ko, D. Pagan, J. Neuefeind, W. J. Weber, and Y. Zhang, Local Structure and Short-Range Order in a NiCoCr Solid Solution Alloy, Phys. Rev. Lett. **118**, 205501 (2017).

[22] Y. Zhang, Y. J. Zhou, J. P. Lin, G. L. Chen, and P. K. Liaw, Solid-solution phase formation rules for multi-component alloys, Adv. Eng. Mater. **10**, 534 (2008).

[23] S. Banerjee and A. K. Raychaudhuri, Electrical resistivities of γ-phase $Fe_xNi_{80-x}Cr_{20}$ alloys, Phys. Rev. B **50**, 8195 (1994).

[24] T. K. Nath and A. K. Majumdar, Resistivity saturation in substitutionally disordered γ-$Fe_{80-x}Ni_xCr_{20}$ $(14 \leqslant x \leqslant 30)$ alloys, Phys. Rev. B **53**, 12148 (1996).

[25] Y. Zhang, G. M. Stocks, K. Jin, C. Lu, H. Bei, B. C. Sales, L. Wang, L. K. Béland, R. E. Stoller, G. D. Samolyuk, M. Caro, A. Caro, and W. J. Weber, Influence of chemical disorder on energy dissipation and defect evolution in concentrated solid solution alloys, Nat. Commun. **6**, 8736 (2015).

[26] K. Jin, B. C. Sales, G. M. Stocks, G. D. Samolyuk, M. Daene, W. J. Weber, Y. Zhang, and H. Bei, Tailoring the physical properties of Ni-based single-phase equiatomic alloys by modifying the chemical complexity, Sci. Rep. **6**, 20159 (2016).

[27] H.-P. Chou, Y.-S. Chang, S.-K. Chen, and J.-W. Yeh, Microstructure, thermophysical and electrical properties in Al_xCoCrFeNi $(0 \leqslant x \leqslant 2)$ high-entropy alloys, Mater. Sci. Eng. B **163**, 184 (2009).

[28] Y.-F. Kao, S.-K. Chen, T.-J. Chen, P.-C. Chu, J.-W. Yeh, and S.-J. Lin, Electrical, magnetic, and Hall properties of Al_xCoCrFeNi high-entropy alloys, J. Alloy Compd. **509**, 1607 (2011).

[29] G. D. Samolyuk, S. Mu, A. F. May, B. C. Sales, S. Wimmer, S. Mankovsky, H. Ebert, and G. M. Stocks, Temperature dependent electronic transport in concentrated solid solutions of the 3d-transition metals Ni, Fe, Co and Cr from first principles, Phys. Rev. B **98**, 165141 (2018).

[30] O. Schneeweiss, M. Friak, M. Dudová, D. Holec, M. Sob, D. Kriegner, V. Holy, P. Beran, E. P. George, J. Neugebauer, and A. Dlouhý, Magnetic properties of the CrMnFeCoNi high-entropy alloy, Phys. Rev. B **96**, 014437 (2017).

[31] J. I. Lee, H. S. Oh, and E. S. Park, Manipulation of $\sigma y/\kappa$ ratio in single phase fcc solid-solutions, Appl. Phys. Lett. **109**, 061906 (2016).

[32] C. Niu, C. R. LaRosa, J. Miao, M. J. Mills, and M. Ghazisaeidi, Magnetically-driven phase transformation strengthening in high entropy alloys, Nat. Commun. **9**, 1363 (2018).

[33] S. Mu, J. Yin, G. D. Samolyuk, S. Wimmer, Z. Pei, M. Eisenbach, S. Mankovsky, H. Ebert, and G. M. Stocks, Hidden Mn magnetic-moment disorder and its influence on the physical properties of medium-entropy NiCoMn solid solution alloys, Phys. Rev. Mater. **3**, 014411 (2019).

[34] Z. Dong, S. Schönecker, W. Li, D. Chen, and L. Vitos, Thermal spin fluctuations in CoCrFeMnNi high entropy alloy, Sci. Rep. **8**, 12211 (2018).

[35] M. Lucas, L. Mauger, J. Munoz, Y. Xiao, A. Sheets, S. Semiatin, J. Horwath, and Z. Turgut, Magnetic and vibrational properties of high entropy alloys, J. Appl. Phys. **109**, 07E307 (2011).

[36] B. C. Sales, K. Jin, H. Bei, G. M. Stocks, G. D. Samolyuk, A. F. May, and M. A. McGuire, Quantum critical behavior in a concentrated ternary solid solution, Sci. Rep. **6**, 26179 (2016).

[37] K. Jin, S. Mu, K. An, W. D. Porter, G. D. Samolyuk, G. M. Stocks, and H. Bei, Thermophysical properties of Ni-containing single-phase concentrated solid solution alloys, Mater. Des. **117**, 185 (2017).

[38] Z. Wu, H. Bei, G. M. Pharr, and E. P. George, Temperature dependence of the mechanical properties of equiatomic solid solution alloys with face-centered cubic crystal structures, Acta Mater. **81**, 428 (2014).

[39] F. Tian, L. K. Varga, N. Chen, L. Delczeg, and L. Vitos, Ab initio investigation of high-entropy alloys of 3d elements, Phys. Rev. B **87**, 075144 (2013).

[40] P. Singh, A. V. Smirnov, and D. D. Johnson, Atomic short-range order and incipient long-range order in high-entropy alloys, Phys. Rev. B **91**, 224204 (2015).

[41] Z. Rao, B. Dutta, F. Körmann, D. Ponge, L. Li, J. He, L. Stephenson, L. Schäfer, K. Skokov, O. Gutfleisch, D. Raabe, and Z. Li, Unveiling the mechanism of abnormal magnetic behavior of FeNiCoMnCu high-entropy alloys through a joint experimental-theoretical study, Phys. Rev. Mater. **4**, 014402 (2020).

[42] D. D. Belyea, M. S. Lucas, E. Michel, J. Horwath, and C. W. Miller, Tunable magnetocaloric effect in transition metal alloys, Sci. Rep. **5**, 15755 (2015).

[43] J. Rodrıguez-Carvajal, Recent advances in magnetic structure determination by neutron powder diffraction, Physica B **192**, 55 (1993).

[44] P. Bag, W. Z. Liu, Y. K. Kuo, C. N. Kuo, and C. S. Lue, Thermoelectric properties of chemically substituted Heusler-type $Ru_{2-x}Nb_{1-x}Ga$ and $Ru_2NbGa_{1-x}M_x$ (M = In, Ge, and Sn) alloys, J. Alloys Compd. **849**, 156617 (2020).

[45] S. Guo, C. Ng, J. Lu, and C. Liu, Effect of valence electron concentration on stability of fcc or bcc phase in high entropy alloys, J. Appl. Phys. **109**, 103505 (2011).

[46] S. Guo, C. Ng, Z. Wang, and C. Liu, Solid solutioning in equiatomic alloys: Limit set by topological instability, J. Alloy Compd. **583**, 410 (2014).

[47] Y. Tong, S. Zhao, K. Jin, H. Bei, J. Y. P. Ko, Y. Zhang, and F. X. Zhang, A comparison study of local lattice distortion in $Ni_{80}Pd_{20}$ binary alloy and FeCoNiCrPd high-entropy alloy, Scr. Mater. **156**, 14 (2018).

[48] Y. Tong, K. Jin, H. Bei, J. Ko, D. C. Pagan, Y. Zhang, and F. Zhang, Local lattice distortion in NiCoCr, FeCoNiCr and FeCoNiCrMn concentrated alloys investigated by synchrotron x-ray diffraction, Mater. Des. **155**, 1 (2018).

[49] C.-W. Tsai, Y.-L. Chen, M.-H. Tsai, J.-W. Yeh, T.-T. Shun, and S.-K. Chen, Deformation and annealing behaviors of high-entropy alloy $Al_{0.5}$CoCrCuFeNi, J. Alloys Compd. **486**, 427 (2009).

[50] P. P. Bhattacharjee, G. D. Sathiaraj, M. Zaid, J. R. Gatti, C. Lee, C. W. Tsai, and J. W. Yeh, Microstructure and texture evolution during annealing of equiatomic CoCrFeMnNi high-entropy alloy, J. Alloys Compd. **587**, 544 (2014).

[51] Y. Feng, B. Zhan, J. He, and K. Wang, The double-wire feed and plasma arc additive manufacturing process for deposition

in Cr-Ni stainless steel, J. Mater. Process. Technol. **259**, 206 (2018).

[52] A. Caballero, J. Ding, S. Ganguly, and S. Williams, Wire + Arc Additive Manufacture of 17-4 PH stainless steel: Effect of different processing conditions on microstructure, hardness, and tensile strength, J. Mater. Process. Technol. **268**, 54 (2018).

[53] H. C. Robarts, T. E. Millichamp, D. A. Lagos, J. Laverock, D. Billington, J. A. Duffy, D. O'Neill, S. R. Giblin, J. W. Taylor, G. Kontrym-Sznajd, M. Samsel-Czekała, H. Bei, S. Mu, G. D. Samolyuk, G. Malcolm Stocks, and S. B. Dugdale, Extreme Fermi Surface Smearing in a Maximally Disordered Concentrated Solid Solution, Phys. Rev. Lett. **124**, 046402 (2020).

[54] S. Mu, G. D. Samolyuk, S. Wimmer, M. C. Troparevsky, S. N. Khan, S. Mankovsky, H. Ebert, and G. M. Stocks, Uncovering electron scattering mechanisms in NiFeCoCrMn derived concentrated solid solution and high entropy alloys, Npj Comput. Mater. **5**, 1 (2019).

[55] W. F. Gale, and T. C. Totemeier, eds., *Smithells Metals Reference Book* (Elsevier, Butterworth-Heinemann, Oxford, 2003).

[56] K. H. J. Buschom and N. M. Beekmans, Thermal stability and electronic properties of amorphous Zr-Co and Zr-Ni alloys, Phys. Rev. B **19**, 3843 (1979).

[57] A. K. Sinha, Electrical resistivity, thermoelectric power, and x-ray interference function of amorphous Ni-Pt-P alloys, Phys. Rev. B **1**, 4541 (1970).

[58] Y. K. Kuo, N. Kaurav, W. K. Syu, K. M. Sivakumar, U. T. Shan, S. T. Lin, Q. Wang, and C. Dong, Transport properties of Ti-Zr-Ni quasicrystalline and glassy alloys, J. Appl. Phys. **104**, 063705 (2008).

[59] S. Huang, E. Holmstrom, O. Eriksson, and L. Vitos, Mapping the magnetic transition temperatures for medium- and high-entropy alloys, Intermetallics **95**, 80 (2018).

[60] Y. K. Kuo, K. M. Sivakumar, C. A. Su, C. N. Ku, S. T. Lin, A. B. Kaiser, J. B. Qiang, Q. Wang, and C. Dong, Measurement of low-temperature transport properties of Cu-based Cu-Zr-Ti bulk metallic glass, Phys. Rev. B **74**, 014208 (2006).

[61] L. Bainsla, K. G. Suresh, A. K. Nigam, M. M. Raja, B. S. D. Ch. S. Varaprasad, Y. K. Takahashi, and K. Hono, High spin polarization in CoFeMnGe equiatomic quaternary Heusler alloy, J. Appl. Phys. **116**, 203902 (2014).

[62] D. Rani, J. Kangsabanik, K. G. Suresh, N. Patra, D. Bhattacharyya, S. N. Jha, and A. Alam, Origin of Local Atomic Order and Disorder in $Co_2Fe_{1-x}Cr_xSi$ Heusler Alloys: Theory and Experiment, Phys. Rev. Appl. **10**, 054022 (2018).

[63] Y. P. Lee, K. W. Kim, J. Y. Rhee, and Y. V. Kudryavtsev, Influence of structural disorder on the temperature dependence of the transport and magnetic properties of β-phase Co_xAl_{1-x} alloy films, Phys. Rev. B **59**, 546 (1999).

[64] P. A. Lee and T. V. Ramakrishnan, Disordered electronic systems, Rev. Mod. Phys. **57**, 287 (1985).

[65] M. Gurvitch, Ioffe-Regel criterion and resistivity of metals, Phys. Rev. B **24**, 7404 (1981).

[66] J. H. Mooij, Electrical conduction in concentrated disordered transition metal alloys, Phys. Status Solidi A **17**, 521 (1973).

[67] A. H. Wilson, The electrical conductivity of the transition metals, Proc. R. Soc. A **167**, 580 (1938).

[68] G. D. Samolyuk, C. C. Homes, A. F. May, S. Mu, K. Jin, H. Bei, G. M. Stocks, and B. C. Sales, Optical conductivity of metal alloys with residual resistivities near or above the Mott-Ioffe-Regel limit, Phys. Rev. B **100**, 075128 (2019).

[69] Y. Liu, H. Tan, Z. Hu, B. Yan, and C. Petrovic, Anomalous Hall effect in the weak-itinerant ferrimagnet $FeCr_2Te_4$, Phys. Rev. B **103**, 045106 (2021).

[70] L. Li, T. F. Qi, L. S. Lin, X. X. Wu, X. T. Zhang, K. Butrouna, V. S. Cao, Y. H. Zhang, J. Hu, and S. J. Yuan, P. Schlottmann, L. E. De Long, and G. Cao, Observation of superconductivity and anomalous electrical resistivity in single-crystal Ir_3Te_8, Phys. Rev. B **87**, 174510 (2013).

[71] S. A. Hartnoll, Theory of universal incoherent metallic transport, Nat. Phys. **11**, 54 (2015).

[72] L. Bainsla, M. M. Raja, A. K. Nigam, and K. G. Suresh, CoRuFeX (X = Si and Ge) Heusler alloys: High T_C materials for spintronic applications, J. Alloys Compd. **651**, 631 (2015).

[73] D. Bombor, C. G. F. Blum, O. Volkonskiy, S. Rodan, S. Wurmehl, C. Hess, and B. Buchner, Half-Metallic Ferromagnetism with Unexpectedly Small Spin Splitting in the Heusler Compound Co_2FeSi, Phys. Rev. Lett. **110**, 066601 (2013).

[74] D. Rani, K. G. S. Enamullah, A. K. Yadav, S. N. Jha, D. Bhattacharyya, M. R. Varma, and A. Alam, Structural, electronic, magnetic, and transport properties of the equiatomic quaternary Heusler alloy CoRhMnGe: Theory and experiment, Phys. Rev. B **96**, 184404 (2017).

[75] F. J. Blatt, D. J. Flood, V. Rowe, P. A. Schroeder, and J. E. Cox, Magnon-Drag Thermopower in Iron, Phys. Rev. Lett. **18**, 395 (1967).

[76] T. Bohnert, V. Vega, A.-K. Michel, V. M. Prida, and K. Nielsch, Magneto-thermopower and magnetoresistance of single Co-Ni alloy nanowires, Appl. Phys. Lett. **103**, 092407 (2013).

[77] J. Dolinsek, M. Komelj, P. Jeglic, S. Vrtnik, D. Stanic, P. Popcevic, J. Ivkov, A. Smontara, Z. Jaglicic, P. Gille, and Y. Grin, Anisotropic magnetic and transport properties of orthorhombic $Al_{13}Co_4$, Phys. Rev. B **79**, 184201 (2009).

[78] H. Takahashi, T. Akiba, K. Imura, T. Shiino, K. Deguchi, N. K. Sato, H. Sakai, M. S. Bahramy, and S. Ishiwata, Anticorrelation between polar lattice instability and superconductivity in the Weyl semimetal candidate $MoTe_2$, Phys. Rev. B **95**, 100501(R) (2017).

[79] Y. K. Kuo, K. M. Sivakumar, H. C. Chen, J. H. Su, and C. S. Lue, Anomalous thermal properties of the Heusler alloy $Ni_{2+x}Mn_{1-x}Ga$ near the martensitic transition, Phys. Rev. B **72**, 054116 (2005).

[80] C. S. Lue, C. F. Chen, J. Y. Lin, Y. T. Yu, and Y. K. Kuo, Thermoelectric properties of quaternary Heusler alloys $Fe_2VAl_{1-x}Si_x$, Phys. Rev. B **75**, 064204 (2007).

[81] J. Barth, G. H. Fecher, B. Balke, S. Ouardi, T. Graf, C. Felser, A. Shkabko, A. Weidenkaff, P. Klaer, H. J. Elmers, H. Yoshikawa, S. Ueda, and K. Kobayashi, Itinerant half-metallic ferromagnets Co_2TiZ (Z = Si, Ge, Sn): *Abinitio* calculations and measurement of the electronic structure and transport properties, Phys. Rev. B **81**, 064404 (2010).

[82] A. A. Leino, G. D. Samolyuk, R. Sachan, F. Granberg, W. J. Weber, H. Bei, J. Liu, P. Zhai, and Y. Zhang, GeV ion irradiation of NiFe and NiCo: Insights from MD simulations and experiments, Act. Mater. **151**, 191 (2018).

[83] Y. K. Kuo, K. M. Sivakumar, H. H. Lai, C. N. Ku, S. T. Lin, and A. B. Kaiser, Thermal and electrical transport properties of Ag-In-Yb quasicrystals: An experimental study, Phys. Rev. B **72**, 054202 (2005).

[84] M. N. Baibich, W. B. Muir, Z. Altounian, and T. Guo-Hua, Thermopower and resistivity in amorphous $Mg_{1-x}Zn_x$ alloys, Phys. Rev. B **26**, 2963 (1982).

[85] K. Han, H. Jiang, T. Huang, and M. Wei, Thermoelectric properties of $CoCrFeNiNb_x$ eutectic high entropy alloys, Crystals **10**, 762 (2020).

[86] Y. K. Kuo, K. M. Sivakumar, J. I. Tasi, C. S. Lue, J. W. Huang, S. Y. Wang, D. Varshney, N. Kaurav, and R. K. Singh, The effect of Al/Si ratio on the transport properties of the layered intermetallic compound $CaAl_2Si_2$, J. Phys.: Condens. Matter **19**, 176206 (2007).

[87] Y. Liu, H. Lei, K. Wang, M. Abeykoon, J. B. Warren, E. Bozin, and C. Petrovic, Thermoelectric studies of $Ir_{1-x}Rh_xTe_2$ ($0 \leqslant x \leqslant 0.3$), Phys. Rev. B **98**, 094519 (2018).

[88] E. Mun, H. Ko, G. J. Miller, G. D. Samolyuk, S. L. Budko, and P. C. Canfield, Magnetic field effects on transport properties of $PtSn_4$, Phys. Rev. B **85**, 035135 (2012).

[89] L. Zu, S. Lin, P. Tong, J. C. Lin, X. C. Kan, B. S. Wang, W. H. Song, and Y. P. Sun, Synthesis and physical properties of Cr-P-based intermetallic compounds: Cr_3P, Cr_3PC, and Cr_3PN, J. Alloys Compd. **630**, 310 (2015).

[90] B. C. Sales, J. Yan, W. R. Meier, A. D. Christianson, S. Okamoto, and M. A. McGuire, Electronic, magnetic, and thermodynamic properties of the kagome layer compound FeSn, Phys. Rev. Mater. **3**, 114203 (2019).

[91] Th. Siebold and P. Ziemann, Temperature dependence of the thermoelectric effect of ion-bombarded NbN films: Evidence for the suppression of phonon drag and for renormalization, Phys. Rev. B **51**, 6328 (1995).

[92] I. Knapp, B. Budinska, D. Milosavljevic, P. Heinrich, S. Khmelevskyi, R. Moser, R. Podloucky, P. Prenninger, and E. Bauer, Impurity band effects on transport and thermoelectric properties of $Fe_{2-x}Ni_xVAl$, Phy. Rev. B **96**, 045204 (2017).

[93] C. S. Lue and Y.-K. Kuo, Thermal and electrical transport properties of ordered $FeAl_2$, J. Phys.: Condens. Matter **15**, 877 (2003).

[94] C. N. Kuo, R. Y. Huang, Y. K. Kuo, and C. S. Lue, Transport and thermal behavior of the charge density wave phase transition in CuTe, Phys. Rev. B **102**, 155137 (2020).

[95] S. W. Van Sciver, *Helium cryogenics* (Springer Science & Business Media, New York, 2012).

[96] J. Mucha, H. Misiorek, R. Troć, and Z. Bukowski, Thermal conductivity of $UNi_{0.5}Sb_2$ single crystal, J. Phys.: Condens. Matter **18**, 3097 (2006).

[97] H.-S. Kim, Z. M. Gibbs, Y. Tang, H. Wang, and G. J. Snyder, Characterization of Lorenz number with Seebeck coefficient measurement, Apl. Mater. **3**, 041506 (2015).

[98] B. Ramachandran, P. C. Chang, Y. K. Kuo, and C. S. Lue, Electrical and thermal transport properties of intermetallic $RCoGe_2$ (R = Ce and La) compounds, J. Phys.: Condens. Matter **26**, 255601 (2014).

[99] T. M. Tritt (ed.), *Thermal Conductivity: Theory, Properties, and Applications* (Springer Science & Business Media, New York, 2005).

[100] Y. Sui, S. Gao, X. Chen, J. Qi, F. Yang, F. Wei, Y. He, Q. Meng, and Z. Sun, Microstructures and electrothermal properties of $Al_xCrFeNi$ multi-component alloys, Vacuum **144**, 80 (2017).

[101] F. Antao, M. Dias, J. B. Correia, A. Galatanu, M. Galatanu, U. V. Mardolcar, A. Myakush, M. M. Cruz, A. Casaca, R. C. da Silva, and E. Alves, The effects of mechanical alloying on the physical and thermal properties of CuCrFeTiV alloy, Mater. Sci. Eng., B **263**, 114805 (2021).

[102] A. Karati, M. Nagini, S. Ghosh, R. Shabadi, K. G. Pradeep, R. C. Mallik, B. S. Murty, and U. V. Varadaraju, $Ti_2NiCoSnSb$—a new half-Heusler type high-entropy alloy showing simultaneous increase in Seebeck coefcient and electrical conductivity for thermoelectric applications, Sci. Rep. **9**, 5331 (2019).

[103] K. Gianno, A. V. Sologubenko, M. A. Chernikov, H. R. Ott, I. R. Fisher, and P. C. Canfield, Low-temperature thermal conductivity of a single-grain Y-Mg-Zn icosahedral quasicrystal, Phys. Rev. B **62**, 292 (2000).

[104] P. Tong, Y. P. Sun, X. B. Zhu, and W. H. Song, Strong spin fluctuations and possible non-Fermi-liquid behavior in $AlCNi_3$, Phys. Rev. B **74**, 224416 (2006).

[105] S. Uporov, V. Bykov, S. Estemirova, S. Melchakov, and R. Ryltsev, Electronic transport in equiatomic CuZrNiTi alloy, J. Alloys Compd. **770**, 1164 (2019).

[106] Z. Fan, H. Wang, Y. Wu, X. Liu, and Z. Lu, Thermoelectric performance of PbSnTeSe high-entropy alloys, Mater. Res. Lett. **5**, 187 (2017).

[107] J. Yan, F. Liu, G. Ma, B. Gong, J. Zhu, X. Wang, W. Ao, C. Zhang, Y. Li, and J. Li, Suppression of the lattice thermal conductivity in NbFeSb-based half-Heusler thermoelectric materials through high entropy effects, Scr. Mater. **157**, 129 (2018).

[108] A. Alam and A. Mookerjee, Lattice thermal conductivity of disordered NiPd and NiPt alloys, J. Phys.: Condens. Matter **18**, 4589 (2006).